CFD-SIMULATION OF THE ROTOR HEAD INFLUENCE TO THE ROTOR-FUSELAGE INTERACTION

Ulrich Kowarsch, Manuel Keßler and Ewald Krämer
kowarsch@iag.uni-stuttgart.de, University of Stuttgart, IAG, Pfaffenwaldring 21, Stuttgart, 70569, Germany

Abstract

The presented paper investigates a fluid-structure interaction phenomenon of a helicopter in fast forward flight, called tail shake. Due to the interaction of the rotor wake with the tail boom, a high vibration level is introduced under unfavorable conditions. To achieve a more detailed insight into the main rotor wake structure, a Computational Fluid Dynamics (CFD) simulation of a complete helicopter configuration is performed. Due to the high influence of the main rotor head on the wake structure a, detailed model is considered, including the swashplate and the control rods.

In order to resolve the influence of the components, the configuration of the rotor head is simulated in several variants. Former investigations showed the necessity to ensure a low numerical dissipation to preserve the rotor wake. For this investigation the compact reconstruction fifth order Weighted Essentially Non-Oscillatory fluid state reconstruction scheme for an improved rotor wake conservation is used. In addition, the flux computation is solved using an upwind HLLC Riemann solver.

The analysis of the flow field and forces shows a fundamental change of the unsteady flow behavior. Especially due to interaction effects at the cowling and tail, the character of the incoming flow from the rotor wake has substantial impact. The comparison of the different configurations revealed a strong difference particularly in the low frequency intensity of the wake. Due to the natural frequencies of concern for the dynamic of tail in this low frequency range, the consideration of the rotor hub geometry is essential to investigate rotor-fuselage interaction phenomena with focus on possible dynamic excitation. Therefore, this investigation confirmed the necessity of modeling the rotor hub including the control rods.

1 INTRODUCTION

In the field of the computational fluid dynamics (CFD), interaction phenomena are still a not fully understood issue. In case of helicopter aerodynamics, an interaction phenomenon, which may occur during fast forward flight, is called ”tail shake”[1]. In this flight state, the highly unsteady main rotor wake strikes onto the tail boom and empennage and excites a fluctuation of the lateral bending moment on the helicopter fuselage. If this excitation is close to an elastic mode of the fuselage structure, a high lateral vibration level is caused with undesirable character[1]. Several well known helicopter prototypes as the Boeing AH-64D Longbow Apache[2] and the Eurocopter EC135[3] were affected by this phenomenon. If this issue is not noticed before the early flight test phase, it causes high mitigation efforts and costs owed to extensive wind tunnel or even flight test campaigns to resolve the problem[3].

Too low computational resources and too high numerical dissipation of the vortex structures refused the prediction of this phenomenon using CFD until now. Besides the availability of higher computational resources, the numerics have made progress in the field of higher order methods to increase the vortex preservation. At the Institute for Aerodynamics and Gas Dynamics (IAG) of the University of Stuttgart, this field of research was taken up to be investigated for its application to helicopter simulations. In the course of this, the structured CFD solver FLOWer from the German Aerospace Center[4] was extended with different methods of spatially fifth order Weighted Essentially Non-Oscillatory (WENO) schemes[5;6] to enhance the conservation of the rotor wake on its path to the fuselage interaction. First results of the higher order method in FLOWer for the rotor-fuselage interaction were presented[7]. Significant improvements of the vortex preservation and the reproduction of experimental data were achieved. Moreover, the investigation resolved the high influence of the rotor head to the rotor wake as described in experimental papers[1;3]. Strehlow et al.[8] describe the excitation of the tailboom as two superimposing effects. First the rotor hub and fuselage aftbody wake impingement with the tailboom. Second, a vortex shedding at the fuselage and a resulting lock in phenomena with the dynamic elasticity.

The present paper is focused on the wake impingement especially due to a variation of the rotor hub wake and its influence on the flow field at the tailboom. Therefore, a full scale Eurocopter EC145-C2 helicopter with a detailed rotor head model is simulated. Besides the investigation of the serial rotor head configuration, a variation of the considered

components is performed to resolve their influence on the rotor head wake. To improve the low numerical dissipation originated from the WENO implementation, the CRWENO scheme according to Ghosh[9] is implemented in the FLOWer code. The scheme combines the Compact Reconstruction approach with the robust WENO scheme forming an implicit method of resolution in space, which improves the spectral resolution compared to the standard WENO scheme[9].

2 SETUP AND SIMULATION

For most of the common helicopter simulations, a modeling of the main rotor head is neglected to save computational effort. Especially when using a structured solver as FLOWer, a detailed modeling of complex surfaces can extend the required cell amount and manual work load for the grid generation significantly. In order to resolve the wake characteristics of the main rotor head, a trade off between the level of detail and additional cells has to be made. Figure

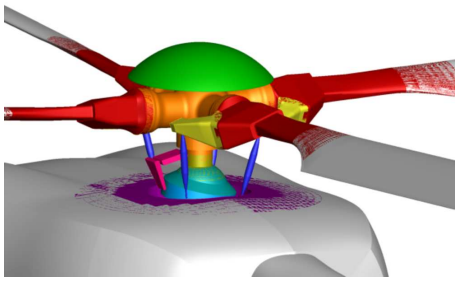

Fig. 1. Approximation of the rotor head geometry with separately meshed components.

1 shows the surface of the approximated rotor head, colored with the separately meshed sections. The rotor head model includes the blade roots (red), rotor mast with the blade connections (orange), control rods (blue) and their connections to the blades (yellow), the swashplate (blue) with its deepening into the fuselage (purple) as well as the scissors (magenta) between swashplate and rotor mast. To simulate the relative motions between the individual parts all components are independently meshed and combined using the chimera technique for overlapping grids. To allow the use of the rotor head meshes for different control angles and the adaption of the movement during trim convergence, the rubber cover between swashplate and rotor mast is modeled as a sphere on which the swashplate can move with its native inclination motion. The vibration absorbers at the blade root were omitted for this investigation.
The extrusion of the body grids was kept as small as possible in close proximity to the surface. At the grid boundary the fluid state is transferred to an automatically created Cartesian background mesh. The coarsening of the background mesh towards the far field was realized by the use of hanging grid nodes. With this approach about 48% of the global cells are located in the Cartesian background mesh with a high cell density in the rotor wake area (cf. Figure 2). This mesh strategy leads a high numerical quality with sparsely skewed and low size ratio grids. The overall basic setup with all components is listed in Table 1. Besides the rotor hub system and the rotor hub wake path in the background, the mesh resolution is held moderate to enable a simulation of different configurations with acceptable computational effort. The block splitting of the grids enables an efficient parallelization of the simulation. The higher order method is applied to the regions of concern, whereas in other regions the second order Jameson Schmidt Turkel (JST) scheme is used to save computational time. These regions of concern contain the rotor head meshes, upper fuselage regions and the background mesh. The landing skids were neglected for this investigation. An elastic modeling of the tail boom was not performed in this simulation.

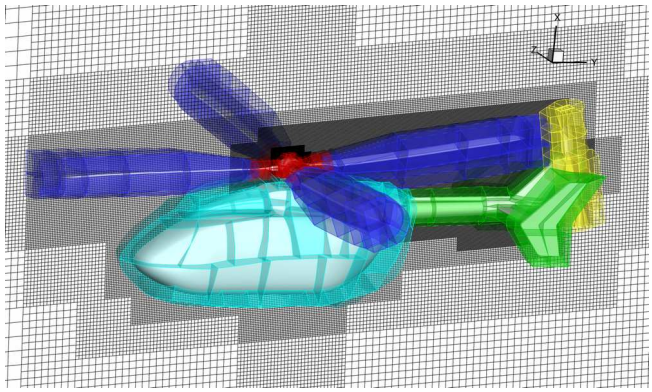

Fig. 2. Simulation setup with the component grids embedded in the Cartesian background mesh.

Component	No. of blocks	No. of cells
Fuselage	205	3,967,232
Main rotor blade	4× 59	4× 1,374,720
Rotorhub system	828	11,935,744
Tail rotor blade	2× 54	2× 1,418,880
Background	1199	19,707,904
Total	**2576**	**43,947,520**

Table 1. Grid system of the baseline CFD setup.

Figure 3 shows the different configurations which were investigated. The baseline setup C-1 is the EC145-C2 serial configuration. The influence of the control rods and scissors is investigated by neglecting them in configuration C-3. Setup C-4 equals setup C-1 without the rotor hub cap. The purpose of this

choice of configurations is less to optimize the geometry of the main rotor hub than to get an insight into the vortex structure formed by the influence of the different rotor hub components. The investigated flight

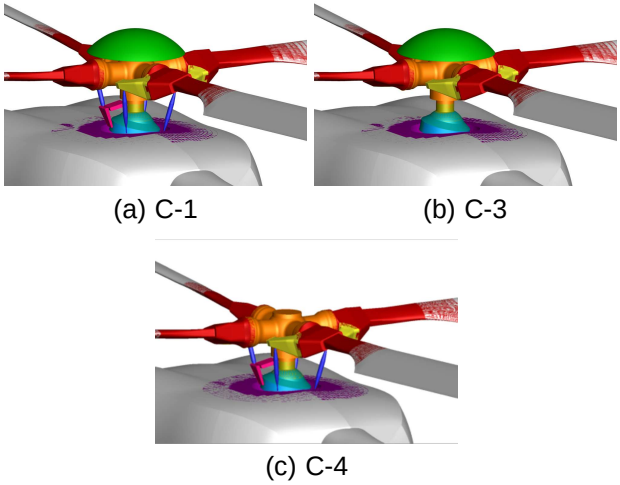

(a) C-1 (b) C-3

(c) C-4

Fig. 3. Configurations of the different test cases.

state is a $120\,\mathrm{kn}$ level flight in an altitude of $7000\,\mathrm{ft}$ with ISA conditions. The couter-clockwise rotating main rotor has 4 blades with a rotation frequency of $6.4\,\mathrm{Hz}$. The two bladed tail rotor has a 5.65 times higher rotation frequency of $36.2\,\mathrm{Hz}$.

As mentioned, the aerodynamic solution is computed with the block structured finite volume Reynolds averaged Navier Stokes (RANS) CFD code FLOWer. The RANS equations are closed using the Wilcox k-ω turbulence model[10]. The time discretization is achieved by merging the governing differential equation in space with the implicit dual time-stepping approach according to Jameson[11].

In the course of this investigation the CRWENO scheme according to Ghosh[9] was implemented into FLOWer for the reconstruction of the convective fluid states at the cell boundaries. The scheme combines the compact reconstruction approach with the robust fifth order WENO scheme, which results in an improved spectral resolution[9]. The method performs well and shows superiority in the efficiency compared to the also implemented standard WENO scheme according to Jiang and Shu[12]. The Riemann problem at the cell boundary is solved using the upwind HLLC scheme according to Toro[13]. The viscous fluxes are solved with central differences of second order accuracy.

For a proper reproduction of the aerodynamics, the dynamic characteristic of the main rotor was considered by a weak fluid-structure coupling between CAMRAD[14] and FLOWer. In addition, CAMRAD ensures the adjustment of the collective and cyclic pitch, the so called trim controls, to meet the required rotor forces and moments for a steady flight state. In this case a wind tunnel trim was performed with a fixed orientation of the fuselage in accordance with the flight data. The trim process was performed for the configuration C-1 and adopted to the other test cases. The motion of the swashplate and control rods system was adapted to meet the updated rotor control angles.

2.1 Simulation and evaluation window

Each simulation was computed for 6 complete rotor revolutions on the basis of the trim convergence results, from which 3 are used to overcome startup effects. With the focus on unsteady behavior of the rotor wake, the time step was set to 0.5° azimuthal resolution. The evaluation thus gives the capability to resolve frequencies up to $360\,{}^{1}/_{\mathrm{rev}}$ according to the Nyquist criterion. The evaluated time window was set to 3 rotor revolutions to map lower frequencies than the main rotor frequency more reliable. This gave a time signal with 2160 time steps. Especially due to the low natural frequencies of the tailboom dynamics in the region of $0.5-2.0$ rotor harmonics (Ω) the consideration of more than one rotor revolution is recommended to resolve the frequencies of relevance for a possible dynamic excitation.

The simulation was performed on the CRAY XE6 Hermit cluster at the High Performance Computing Center (HLRS) in Stuttgart. 1024 cores were used for each computation where each lasted around $150,000$ core hours. The wall clock time was about factor 1.5 higher due to excessive file output.

3 NUMERICAL RESULTS

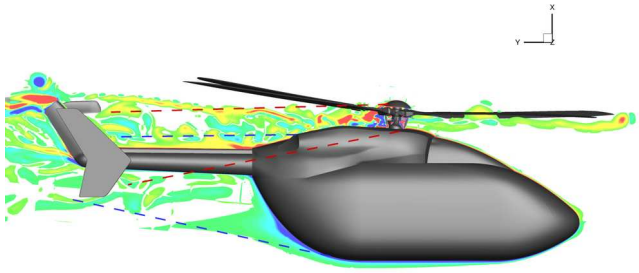

Fig. 4. In-plane vorticity of the symmetry plane (45° azimuth, 6^{th} rotor revolution, setup C-1)

Figure 4 shows the instantaneous in plane voriticy of a slice through the helicopter symmetry plane. Regions without fluid rotation are blanked out. The distinctive turbulence of the rotor wake in the region between hub and tail boom is present. The red dashed line shows the boundaries of the rotor hub wake which is of concern for the tail shake interaction according to[1]. Strehlow et al.[8] classified the tailboom wake

interaction phenomena in two categories. First the interaction with the rotor hub wake and second with the fuselage aft body wake. The two categories of wake are bounded by red dashed lines for the rotor hub wake and blue dashed lines for the fuselage wake. Some overlap between the wakes is present where blending and interaction phenomena are expected. In the course of this investigation, the focus is set to the rotor hub wake, its influence to the fuselage aft body wake, and the resulting force and moment behavior of the tailboom. A more precise characteristic of the rotor hub wake gives the three dimensional flow field in Figure 5. It can be seen, that the wake has a slight tendency to the starboard side and the retreating blade. This can be explained with the high advance ratio of $\mu = 0.31$ in this flight state and the highly detached flow at the blade roots.

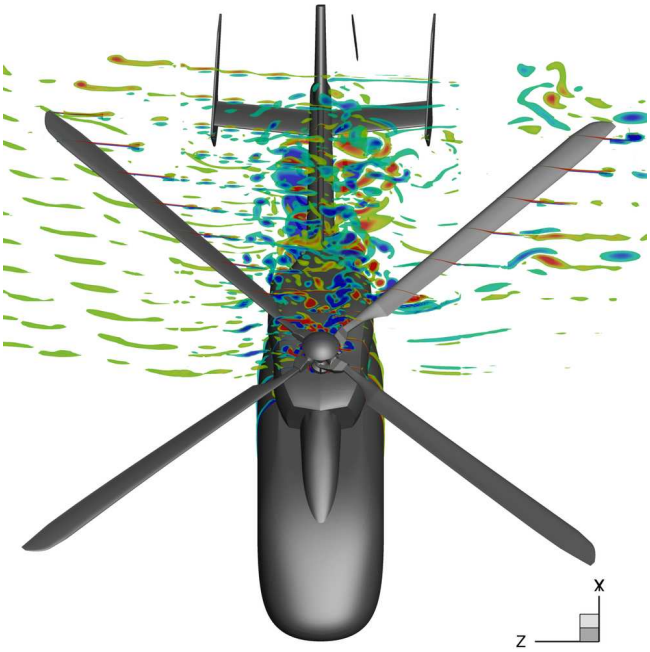

Fig. 5. In-plane vorticity of vertical planes behind the rotor head (45° azimuth, 6^{th} rotor revolution, setup C-1)

The vortex structure is mainly driven by the rotor hub wake, whereas the rotor blade tip wakes show the typical characteristics of defined vortex trajectories. The rotor hub wake shows two strong vortices, which limit the highly turbulent area. In order to gain a detailed insight into the vortex structure the investigation focuses on the unsteady behavior of the rotor wake with regard to low frequency oscillations. The different configurations should enable the assignment of wake phenomena to individual rotor hub geometry elements by comparing them. The mapped time signal over 3 rotor revolutions is therefore transformed into the frequency domain using Direct Fourier Transformation (DFT). To measure non harmonic signal frequencies more reliable, a Hamming window function is applied to the signal as well as zero padding for a more detailed evaluation of the frequency domain signal.

3.1 Flow field phenomena

Former, mainly experimentally based, investigations showed the characteristic influence of rotor hub components to the rotor hub wake[15]. The inclination of the rotor hub wake was found to be mainly driven by the rotor hub cap. The uniformly arranged control rods induce equally to the main rotor blades a 4Ω oscillation, however, with a phase sweep due to their installation. The scissor between rotor mast and swash plate induces a 1Ω component. Besides the fluctuations due to the periodic change of inflow velocity and rotation speed, the physical characteristics of the geometry of the component are relevant considering effects of separation. Especially the control rods show a typical cylindrical shape in their cross-section, from which the formation of a von Kármán vortex street is expected. Hence due to the small diameter high frequencies are expected, which are too high to be relevant for the rotor-fuselage interaction and may not be resolved sufficiently to consider their influence reliably. The frequency of the von Kármán vortex street is estimated with the diameter $d = 0.025\,\mathrm{m}$, the average inflow velocity of $v = 66.8\,\frac{\mathrm{m}}{\mathrm{s}}$ and a blade tip Reynolds number of $Re = 4.2E^6$ leading to a Strouhal number of $Sr = 0.2$ according to [16]. The formula

$$f = Sr\frac{v}{d}, \tag{1}$$

leads to a frequency of the von Kármán vortex street of $534.4\,\mathrm{Hz}$. With the main rotor rotation frequency of $6.4\,\mathrm{Hz}$ and a control rod position outside the axis of rotation of $d = 0.215\,\mathrm{m}$, the frequency of the wake varies with $534.4\,\mathrm{Hz} \pm 69.0\,\mathrm{Hz}$. The grid is designed to preserve wave lengths up to approximately $0.2\,\mathrm{m}$ using a grid resolution of $0.02\,\mathrm{m}$ in the rotor hub wake region. The von Kármán vortex street, in contrast, is expected to have a wave length of $0.13\,\mathrm{m}$. Thus, a detailed resolution of the oscillation induce by the control rods is not expected over a long distance.
Figure 6 shows a slice trough the rotor hub and control rods for different azimuthal positions. The area around the rotor hub is discretized with $0.01\,\mathrm{m}$ to ensure a highly resolved source area of the wake disturbances. Considering the slice at $\Psi = 21^\circ$ the flow around the rotor hub shows the expected characteristics. The retreating control rod shows the formation of a von Kármán vortex street as well as the control rod in the front area. The oscillations of the wake characteristic show the expected wave length with approximately $0.13\,\mathrm{m}$. Hence, the preservation

of the wake could only be obtained for a short distance up to the superposition with the rotor mast wake and the resolution reduction to $0.02\,\mathrm{m}$ behind the rotor hub. The scissor positioned at $\Psi = 21^\circ$ shows its influence to the rotor mast wake, which changes the inclination angle of the wake at the advancing side. At $\Psi = 50^\circ$ the retreating control rod enters the wake area of the rotor mast, which suppresses the formation of the von Kármán vortex street. Hence the strength of the control rod wake is still influencing the wake formation. The same characteristic is found at the advancing side. The significant influence of the scissors to the rotor hub wake is found comparing $\Psi = 21^\circ$ to $\Psi = 264^\circ$, where a substantially changed wake is found especially at the retreating side of the rotor hub. Therefore, a 1Ω influence is expected to be found in the area as well as interaction phenomena between controls rods and scissors.

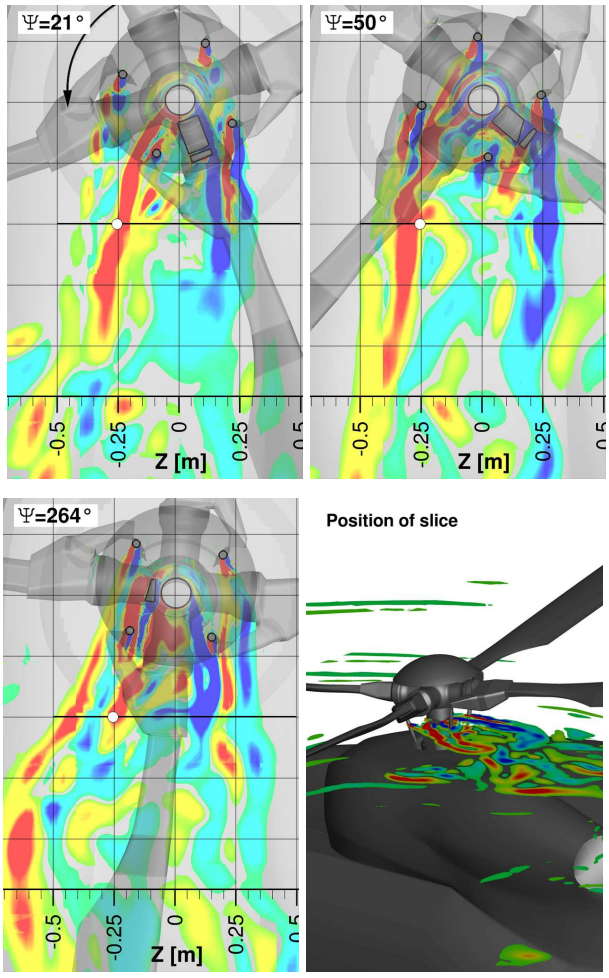

Fig. 6. In-plane vorticity of a slice trough the rotor hub wake

The rotor hub wake directly beyond the hub is investigated by the consideration of the pressure signal monitored at a line trough the wake at $X = -0.15\,\mathrm{m}$ (black line in Figure 6). The time signal over 3 rotor revolutions is transformed to the frequency domain and its pressure amplitude is shown in Figure 7.

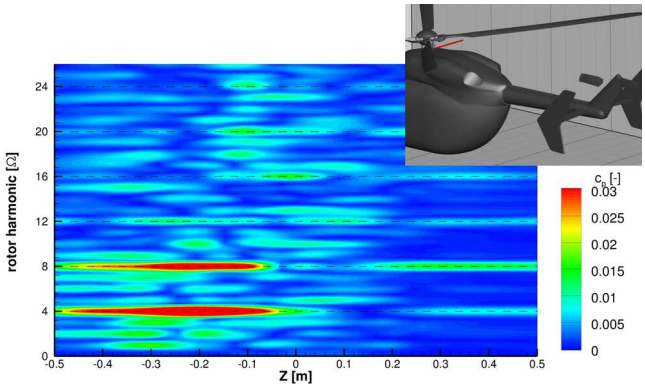

Fig. 7. Frequency spectrum of the pressure signal on a line trough the rotor hub wake ($X = -0.15\,\mathrm{m}$, $Y = 0.5\,\mathrm{m}$)

The plots shows the asymmetry of the wake with its highly unsteady character on the retreating blade side. Primarily the blade passing frequency and its first harmonic is driven. Beside the 1Ω formed by the scissor and the BPF (4Ω) and harmonics of it, several side frequencies occur, which are supposed to result of interference effects of the wake with other components. This assumption is confirmed due to the occurrence of frequencies representing interference frequencies like a 3Ω and 5Ω rotor harmonic frequency, resulting of a nonlinear interaction of a 4Ω and a 1Ω harmonic frequency.
Considering the geometry of the rotor mast, its diameter of $d = 0.1\,\mathrm{m}$ leads according to equation (1) to a frequency of $133.6\,\mathrm{Hz} \approx 21\Omega$ rotor harmonic. Focusing on unsteady characteristics of Figure 8, this frequency is not prominently represented in the frequency spectrum of the wake. This may result due to a suppressed formation of a von Kármán vortex street due to the interactions with the control rod and scissors or its rotation velocity.

For a consideration of the time signal, a sensor at $Z = -0.25\,\mathrm{m}, Y = 0.5\,\mathrm{m}$ located on the formerly considered line is analyzed. Figure 8 gives the time domain signal as well as the frequency domain signal of the measured pressure.
For a separation of the different signal components, the signal parts of the BPF harmonics are plotted in blue and the lower harmonics parts in the range of $0.5 - 3.0\Omega$ are plotted in green. Analyzing in detail the BPF oscillation, the phase relation between rotor blades and control rods is visible. The rotor blades induce a slight pressure fluctuation at $\Psi \approx 50^\circ$, 140°, 230°, and 310° shortly before passing the sensor location. The pressure decreases directly after the mentioned positions, when the wake of the passing control rod is moving over the sensor location.

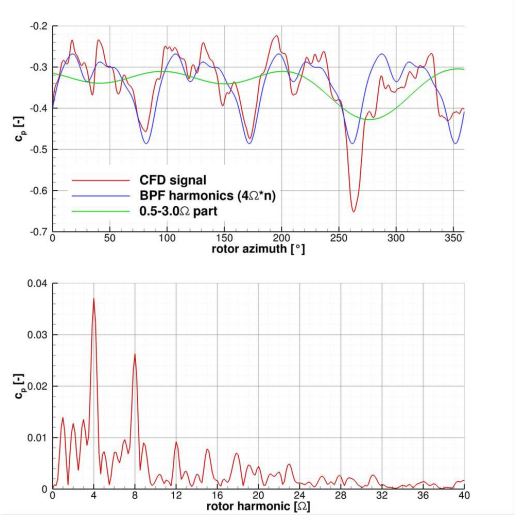

Fig. 8. Frequency spectrum of the pressure signal behind the rotor hub located at $X = -0.15\,\mathrm{m}$, $Y = 0.5\,\mathrm{m}$ (cf. figure 6)

Beside high frequency fluctuations, a strong pressure drop at $\Psi \approx 270^\circ$ is present, which is driven by low harmonic frequencies as plotted in Figure 8. This position coincides with the scissors located indirect proximity in front of the considered sensor. The low pressure signal is explainable by the wake dent due to pressure loss at the flow past the scissor.

3.2 Component loads

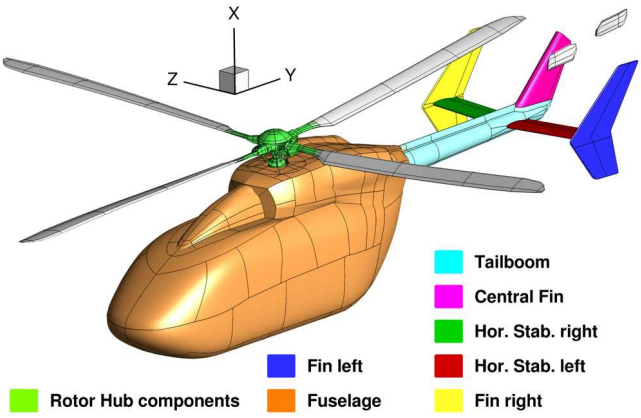

Fig. 9. Surface distribution and notation of components

Figure 10 and 11 gives an overview of the lift and drag forces for the helicopter components in the considered flight state for setup C-1. The distribution of the helicopter surface into the components is given in Figure 9. The main and tail rotor forces are excluded. The rotor hub components are assembled with the rotor hub itself, representing the rotor mast,

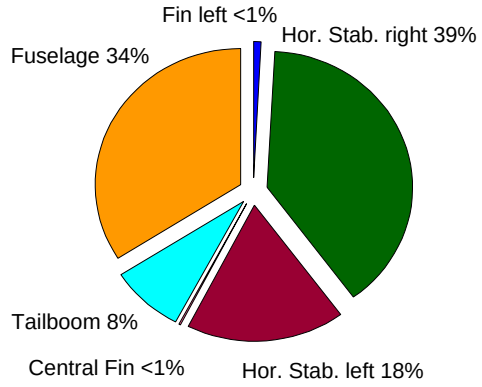

(a) downthrust $-F_X$

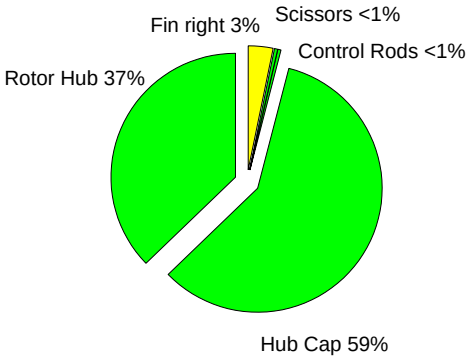

(b) lift F_X

Fig. 10. Downforce and lift loads of the components (ratio 9:1)

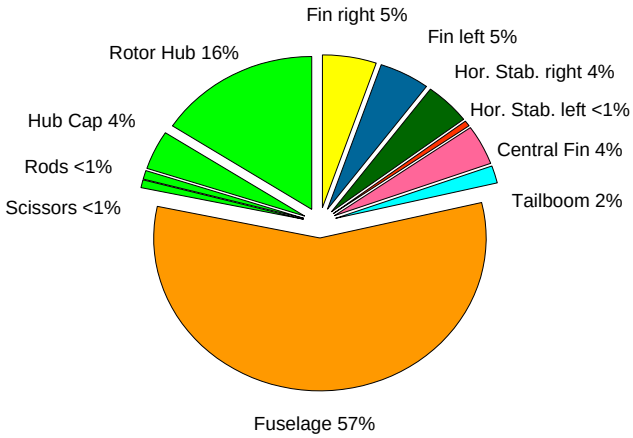

Fig. 11. Drag loads F_Y of components

blade connections, swash plate, and as further components the hub cap, scissors, and control rods. The forces are computed in the fuselage system, in which the main rotor mast has a 5° inclination in positive rotation around the z-axis. The comparison of the component lift forces displays a high percentage of the fuselage and tailboom surface to the downforce. Markable are the downforce of the two horizontal stabilizers to achieve a pitching moment. The starboard side located horizontally has a more than 2 times higher force compared to the backboard sided. The lower downwash at the retreating side of the main rotor causes a lower effective angle of attack resulting in this difference compared to the starboard side. The lift of the considered components is only slightly more than a tenth of the downthrust force and mainly characterized by the rotor hub components. The highest percentage contributes the rotor hub cap followed by the rotor hub, which includes the blade roots.
The parasitic drag (cf. Figure 11) is mostly driven by the fuselage with 57%. The other non-rotating components like the horizontal stabilizer and tailboom contribute 20% and the rotating rotor hub parts in summary 23%, mainly by the rotor hub and hub cap. The drag load of the control rods and scissors play a minor role. Hence, further investigations show their significant influence to wake and, therefore, to the flow field in the aft fuselage and tailboom area.

3.3 Comparison of configurations

The following sections compare the three configurations to resolve the influence of the rotor head components to the main rotor wake.

3.3.1 Unsteady rotor wake characteristics

For the considered helicopter type, the natural frequency of concern for the tail shake behavior is the region of the first main rotor harmonic (1Ω). To investigate the flow behavior in this frequency region, Figure 12 shows the spectral intensity of the pressure oscillation in the frequency range of $0.5\Omega - 2.0\Omega$ for a point cloud in the area of concern (bounded by the grey box). The size and color of the points correlate with the value of intensity, whereby in areas with insignificant spectral excitation the points degrade to zero size. Remarkable is the significant difference in the low frequency spectral intensity between the setups. Focusing on the starboard horizontal stabilizer, setup C-1 shows a significant high intensity at the lower side. The surrounding area shows a comparable behavior between setup C-3 and C-4, whereas setup C-1 differs in the low frequency spectrum. The characteristic of this region is found to be significantly driven by a detached vortex at the fuselage convecting to the horizontal stabilizer. This coincides with

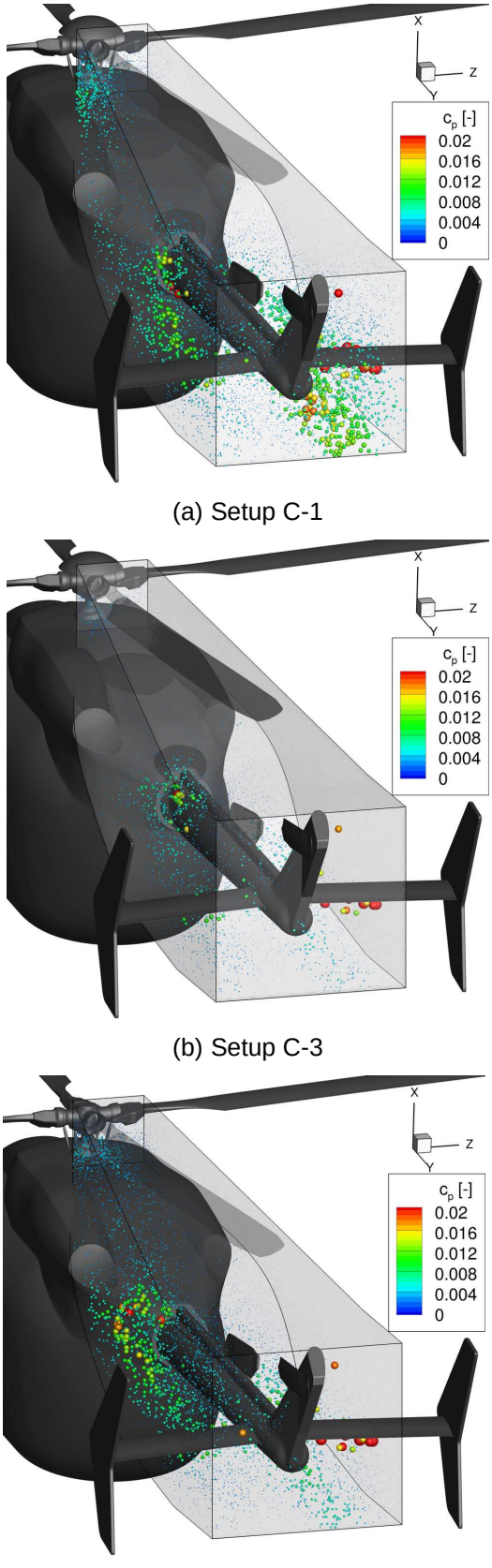

(a) Setup C-1

(b) Setup C-3

(c) Setup C-4

Fig. 12. Spectral intensity of the pressure oscillation in the frequency range of $0.5\Omega - 2.0\Omega$

the classification of tailboom influence by the fuselage wake made by Strehlow et al.[8]. Figure 13 shows an

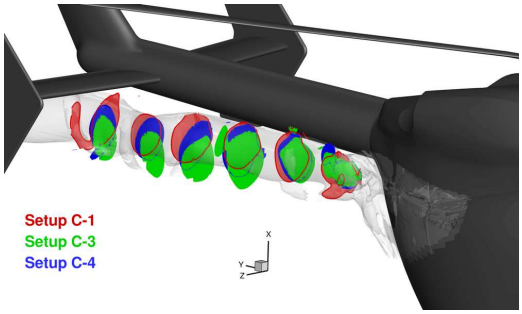

Fig. 13. Vortex location of the detached vortex at the fuselage tailgate detected with the λ_2 criterion

instantaneous visualization of the position of this detached vortex for the different setups. The comparison resolves a variation in the vertical location of the vortex. In case of setup C-1 a higher location is observable whereas setup C-3 has the lowest position. Setup C-1 shows a secondary vortex forming under the horizontal stabilizer which indicates stronger interaction effects than in the other setups. This interaction between horizontal stabilizer and vortex seems to be the trigger for low harmonic fluctuations, since the surrounding area, as well as the detached vortex directly behind the fuselage aft body, do not evince this magnitude of intensity.

A comparable flow state can be found at the collar between fuselage and the tailboom. The separation effects at the engine cowling area and tailboom root differ in their low frequency intensity. In this case setup C-4 has the highest excitation whereas setup C-3 possesses only minor intensity. This allows the conclusion, that non linear interaction phenomena between the cowlings and rotor hub wake lead to interaction frequencies in low frequency areas.

In the region directly behind the rotor hub Figure 12 depicts the high influence of the rods to lower harmonic frequencies, even more prominently found with the scissors. Slight fluctuations occur in case of setup C-3, which are traced back to the inclination of the rotatory part of the swash plate resulting in slightly 1Ω detaching effects. Setup C-1 and C-4 feature significantly stronger low frequency parts in the area of the rotor hub wake.

The analysis results in a significant influence of the rotor hub wake not only to rotor hub close areas, but also to side effects due to interactions in the rotor wake path. The comparison demonstrates the strong influence of minor rotor hub components to the overall flow characteristic at the tailboom. Due to the neglected skids, the flow situation may change at fuselage aft body and the detached vortex formation and convection. Further investigation focusing on comparisons with experimental data will, therefore, include the helicopter skids.

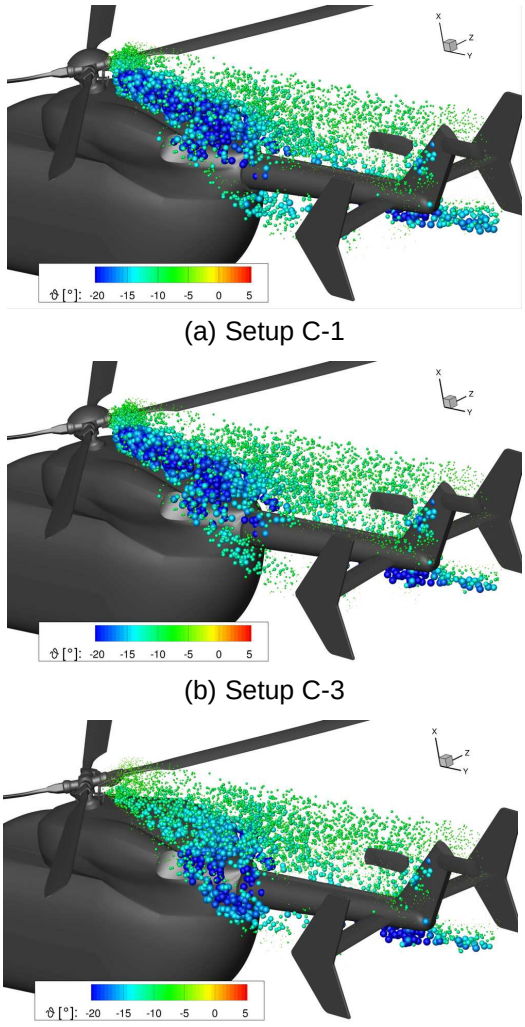

(a) Setup C-1

(b) Setup C-3

(c) Setup C-4

Fig. 14. Time averaged flow angle relative to horizontal plane for a point cloud located in the main rotor wake

The influence of the rotor hub cap is evidenced by the consideration of the rotor wake inclination based on the flow angle relative to the horizontal plane (cf. Figure 14). The flow inclination angle is computed for a point cloud using

$$\vartheta = \arctan\left(\frac{u}{v}\right), \tag{2}$$

with u as the velocity component directed in positive X- and v to positive Y-direction. Setup C-1 and C-3 have a comparable flow characteristic behind the rotor hub with a strong downward trend of the flow. However, setup C-4 has a significantly smaller inclination directly behind the rotor head. This behavior stands in direct connection with the higher spreading of low frequency fluctuations in Figure 12, where a more compact region is found in setup C-1 compared

to C-4 with the same rod components. This shows the influence of the rotor hub cap to the wake characteristic by keeping it more compact in its expansion.
The flow inclination is achieved by a *open* hub cap, which means, that a thin sphere surface is covering the rotor hub (cf. Figure 15). The open volume causes a highly separated flow inside the hub cap which leads in combination with the top flow to a strong flow inclination of the wake. In case of the configuration without hub cap only a slight flow inclination is present (cf. Figure 15) which is caused by the rotor downwash. The missing hub cap reduces the parasitical drag by 5.7% in setup C-4 whereas the hub cap drag portion is 3.9% in setup C-1 with an L/D ratio of 2.95 (cf. Figure 10 and 11). Apart from the higher drag, the hub cap shows a positive influence in the engine cowling and tailboom separation area regarding low frequency excitation. Therefore, the higher flow inclination shows significant influence to the rotor wake for a cost of low additional parasitical drag.

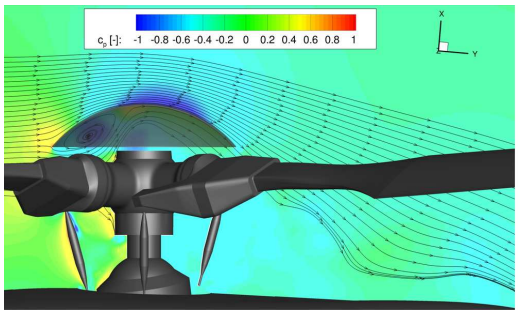

(a) Setup C-1

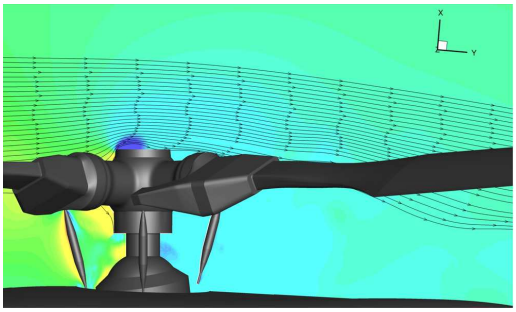

(b) Setup C-4

Fig. 15. Instantaneous flow field around the hub cap at $\Psi = 45°$ (Slice at symmetry plane $Z = 0m$)

3.3.2 Surface pressure distribution

Based on the formerly shown low frequency parts in the rotor hub wake, Figure 16 gives the spectral intensity of the pressure oscillation in the frequency range of $0.5\Omega - 2.0\Omega$ on the fuselage surface. The found characteristic of the rotor hub wake is reflected in the consideration of the surface pressure fluctuations. The low frequency parts around the rotor hub

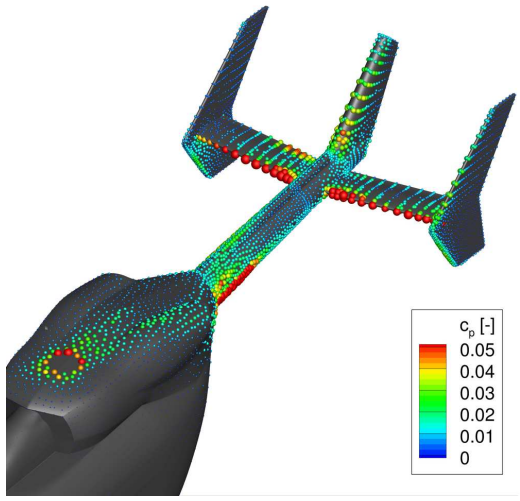

(a) Setup C-1

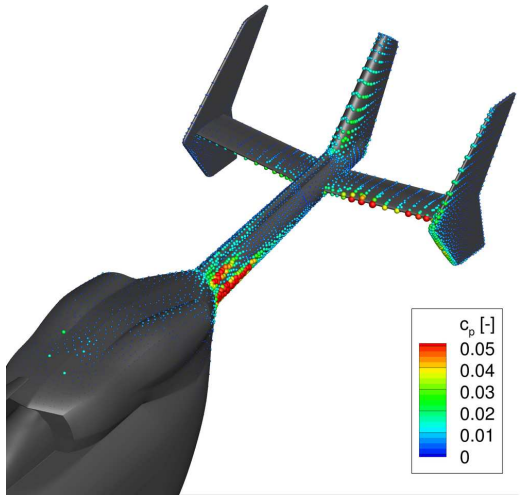

(b) Setup C-3

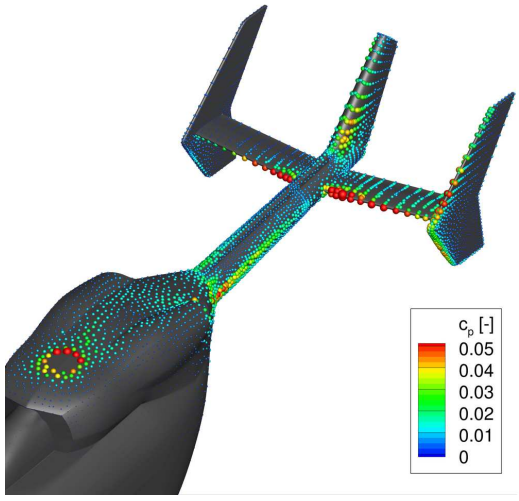

(c) Setup C-4

Fig. 16. Spectral intensity of the pressure oscillation in the frequency range of $0.5\Omega - 2.0\Omega$ on the fuselage surface

is found in the same manner as in Figure 12 for the three setups. One remarkable effect is the spreading of the fluctuation over the lateral axis of the rotor hub wake fluctuations in case of C-4 behind the rotor hub. Setup C-1 shows a higher asymmetry with a concentration of the low frequency behavior at the retreating blade side. This characteristic is traced back to the missing rotor hub cap which shows a stronger flow inclination directly behind the rotor hub. The asymmetric rotor hub is, therefore, projected onto the fuselage surface in its structure whereas the missing hub cap and lower flow inclination allows a wider spreading in case of setup C-4 with slightly lower intensity.
A region of strong low frequency excitation is also found in the area of the front tailboom, which is formed by a detaching phenomenon at the collar between tailboom and fuselage. The strength of this detaching phenomenon in the low frequencies seems to correlate with the flow inclination and, therefore, pressure level in this area, which is driven by the rotor hub cap. Setup C-1 and C-3 have a significantly higher unsteady intensity by a factor of $2-3$. Besides this detaching phenomenon, setup C-1 and C-4 show a higher intensity over the complete tailboom until the horizontal stabilizer. The central fin also exposed to strong low frequencies pressure oscillations due to interaction phenomena with the main rotor wake.
At the starboard horizontal stabilizer the analyzed detached vortex location in Figure 13 explains its influence to the surface pressure fluctuation. Setup C-1 which has the vortex passing closest under the starboard horizontal stabilizer, indicates significant higher low frequency fluctuations than the other cases. Therefore, a low frequently torsion moment at the tailboom is expected. The comparison reveals the significant influence of the control rods to the pressure fluctuations on the surface. Consequently, a direct influence to the loads is expected as well.

3.3.3 Fuselage forces and moments

Figure 17 depicts the frequency spectrum of the integral forces acting on the fuselage including the tailboom components and tail rotor thrust. The lines are slightly shifted for clarity. Considering the vertical force F_X, lower frequencies in the range of $0.25\Omega - 2\Omega$ occur clearly higher in case of setup C-1. Especially in the vertical component F_X this low frequencies are traced back to the found low frequency interaction of a detached vortex at the starboard horizontal stabilizer. The influence of the rotor hub cap shows a reduction of the 4Ω frequency in the vertical force due to the changed rotor wake inclination. The comparison between setup C-1 and C-4 evince a reduction for about 20%. The $\sim 11.3\Omega$ frequency present equals the blade passing frequency of the tail rotor and shows only minor influence on the vertical force fluctuation.

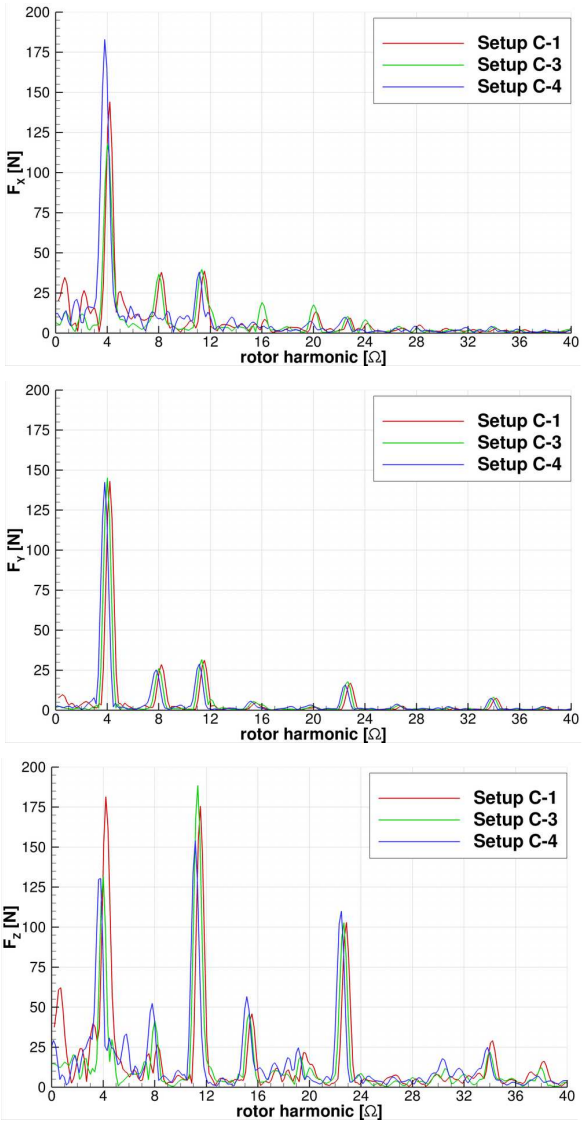

Fig. 17. Frequency spectrum of the forces acting on the non rotating helicopter components incl. Tailrotor

The longitudinal force F_Y has no unexpected characteristic of its frequency spectrum. All three setups have the same frequency components and magnitude of the amplitudes with negligible deviations. The occurring frequencies are the main rotor BPFs and the tail rotor BPFs.
Contrary to the vertical and longitudinal forces, the lateral force F_Z shows a significantly higher unsteady character in all three setup cases. The most prominent frequency occurring is the tail rotor BPF which has its thrust direction in F_Z. Besides the main rotor harmonic, interaction frequencies between main and tail rotor are present as the $\sim 15\Omega$ rotor harmonic in F_Z. In addition to the harmonics of main and tail rotor frequencies, low frequencies occur in the configuration. The highest amplitude is found in setup C-1 with a frequency in the range of 0.75Ω.
Considering the loads onto the surface components

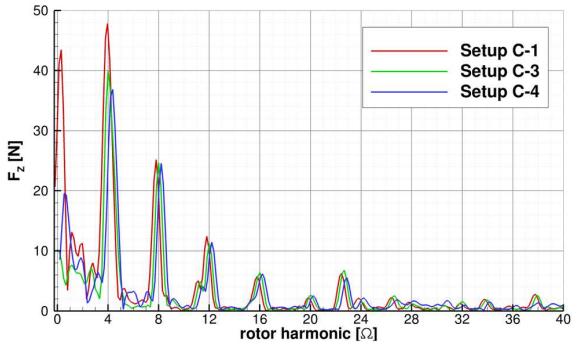

Fig. 18. Frequency spectrum of the lateral force at the tailboom component (cf. Figure 9)

of the fuselage, the most prominent low harmonic fluctuation of the lateral force F_Z in setup C-1 is found at the tailboom component (cf. Figure 9). Figure 18 displays the frequency spectrum which has an amplitude of $\sim 42\,\mathrm{N}$ at the frequency of concern in setup C-1. Compared to the integral force with an amplitude of $\sim 60\,\mathrm{N}$, $\sim 70\,\%$ of the low harmonic fluctuation in the lateral direction occur at the tailboom component specified in Figure 9. The other setups show the same proportion of $\sim 70\,\%$ of amplitude in this low harmonic range, however, with a clearly lower absolute amplitude.

To consider the points of force application of the loads, the moments on the non rotating components inclusive tail rotor are computed. The origin of the reference systems is placed under to rotor head in a fictional center of gravity with the rotor mast as vertical axis. The lateral bending moment M_X is displayed in Figure 19.

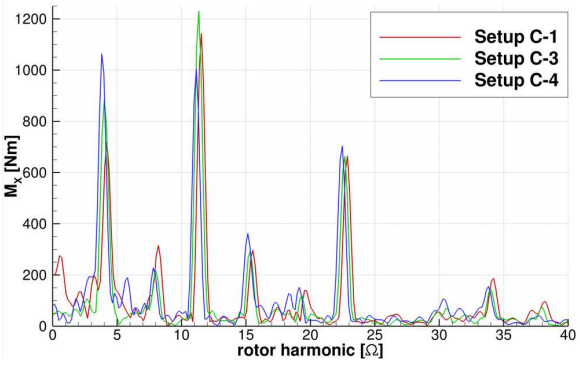

Fig. 19. Frequency spectrum of the vertical moment acting on the non rotating helicopter components incl. Tailrotor around the rotor mast

The long lever arm and thrust direction of the tail rotor is directly reflected in the considered moment. Therefore, the most prominent frequency occurring is the first BPF of the tail rotor (11.3Ω). In addition, the interaction frequencies of main and tail rotor are notable in the moment. Notable is also the higher main rotor BPF influence to the moment in case of setup C-4, which is not directly seen in the lateral forces. This concludes, that due to the changed flow inclination, most main rotor - tail interaction phenomena occur in the more rearward section of the tail as the fins. Considering the low frequency range, C-1 has a higher amplitude by factor 2. Especially in the region of 0.75Ω, the former found influence is reflected in moment in the same manner.
The evaluation concludes that lower frequencies shape the lateral moment in dependency of the configuration which is attributed to be the most important influence for the flow induced fuselage vibration in case of tail shake condition.

4 CONCLUSION AND FURTHER WORK

The paper has presented the investigation of different geometrical rotor hub configurations and their influence on the rotor wake. The comparison showed, that the rod components have only minor influence to the direct hub wake, which, however, triggers interaction phenomena of the wake differently. This change in the rotor hub wake causes significant influence to separation or vortex location effects in the flow convection to the vicinity of the tail. Therefore, force and moments acting on the surface are influenced substantially. The influence of the rotor hub cap has shown to have a high impact on the wake inclination, yet no fundamental change in the spectral intensity of the lower frequency band around the first rotor harmonic is found. These lower harmonic effects are mostly triggered by the turbulence level of the rotor hub wake as it was seen in case the configuration without rotor hub rods.
The investigation confirmed the need of a detailed rotor hub model and the control rod system in the hub area. In addition, higher order methods are required to guarantee a conservation of the wake structure as detailed as possible.
Further investigation in this field of research are focused on an experimentally based flight state and data. To map the separation effects on the fuselage more precisely, skids and an engine boundary condition for a mass and heat entry are to be taken into account. To consider the aeroelasticity of the tailboom structure, a strong coupling between the aerodynamics and structural dynamics of the tailboom is striven. Hereby possible dynamic effects found in previous investigations, like the lock-in phenomenon, may be resolved. In addition, further numerical methods like Detached Eddy Simulations are evaluated to be used for further rotor-fuselage interactions investigations.

REFERENCES

[1] de Waard, P., *Tail Shake Vibration: Objective Comparison of Aerodynamic Configurations in a Subjective Environment*, NLR TP: Nationaal Lucht- en Ruimtevaartlaboratorium, National Aerospace Laboratory, Netherlands, 1999.

[2] Hassan, A., Thompson, T., Duque, E., and Melton, J., “Resolution of Tail Buffet Phenomenon for AH-64DTM Longbow Apace,” Proceedings of the 53rd Annual Forum of the American Helicopter Society, Virginia Beach, VA, 1997.

[3] Kampa, K., Enenkl, B., Polz, G., and Roth, G., “Aeromechanic Aspects in the Design of the EC135,” Proceedings of the 23rd European Rotorcraft Forum, Dresden, 1997.

[4] Kroll, N., Eisfeld, B., and Bleeke, H., “The Navier-Stokes code FLOWer,” *Notes on Numerical Fluid Mechanics*, 1999, pp. 58–71.

[5] Flad, D., *Implementation of a higher order method for flux calculation in FLOWer*, Studienarbeit, Universität Stuttgart, Fakultät Luft- und Raumfahrttechnik und Geodäsie, Institut für Aerodynamik und Gasdynamik, Oktober 2011.

[6] Kowarsch, U., Oehrle, C., Hollands, M., Keßler, M., and Krämer, E., *High Performance Computing in Science and Engineering 13*, Springer Verlag, 2013, Chapter Computation of Helicopter Phenomena Using a Higher Order Method, pp. 423–438.

[7] Kowarsch, U., Keßler, M., and Krämer, E., “High order CFD-simulation of the rotor-fuselage interaction,” 39th European Rotorcraft Forum, Moscow, 2013.

[8] Strehlow, H., Teves, D., and Polz, G., “Applied helicopter aeroelastics : modelling and testing,” Proceedings of the 22nd European Rotorcraft Forum, Brighton, UK, 1996.

[9] Ghosh, D., *Compact-Reconstruction Weighted Essentially Non-Oscillatory Schemes for Hyperbolic Conservation Laws*, Ph.D. thesis, University of Maryland, College Park, MD, 2013.

[10] Wilcox, D., “Multiscale Model for Turbulent Flows,” *AIAA Journal*, Vol. 26, No. 11, 1988, pp. 1311–1320.

[11] Jameson, A., “Time dependent calculations using multigrid, with applications to unsteady flows past airfoils and wings,” AIAA 10th Computational Fluid Dynamics Conference, Honolulu, HI, 1991.

[12] Jiang, G.-S. and Shu, C.-W., “Efficient Implementation of Weighted ENO Schemes,” *Journal of Computational Physics*, Vol. 126, 1996, pp. 202–228.

[13] Toro, E. F., *Riemann Solvers and Numerical Methods for Fluid Dynamics*, Springer Verlag, Berlin, 1997.

[14] Johnson, W., *CAMRAD II Comprehensive analytical model of rotorcraft aerodynamics and dynamics*, fourth edition, 2009.

[15] Sheridan, P. F. and Smith, R. P., “Interactional Aerodynamics - A New Challenge to Helicopter Technology,” Proceedings of the American Helicopter Society, 35th Annual Forum, Washington, D.C, May 1979.

[16] Roshko, A., “Experiments on the Mean Flow Past a Circular Cylinder at Very High Reynolds Number,” *Journal of Fluid Mechanics*, Vol. 10, 1961, pp. 345–356.